RSC Advances

PAPER

View Article Online
View Journal | View Issue

Cite this: *RSC Adv.*, 2020, **10**, 27728

Thermally reduced mesoporous manganese MOF @reduced graphene oxide nanocomposite as bifunctional electrocatalyst for oxygen reduction and evolution†

Abdul Wahab,*[a] Naseem Iqbal,*[a] Tayyaba Noor,[b] Sheeraz Ashraf,[a] Muhammad Arslan Raza,[a] Awais Ahmad[a] and Usman Ali Khan[a]

Received 10th May 2020
Accepted 15th July 2020

DOI: 10.1039/d0ra04193a

rsc.li/rsc-advances

Oxygen electrocatalysis plays a crucial role in harnessing energy from modern renewable energy technologies like fuel cells and metal–air batteries. But high cost and stability issues of noble metal catalysts call for research on tailoring novel metal–organic framework (MOF) based architectures which can bifunctionally catalyze O_2 reduction and evolution reactions (ORR & OER). In this work, we report a novel manganese MOF @rGO nanocomposite synthesized using a facile self-templated solvothermal method. The nanocomposite is superior to commercial Pt/C catalyst both in material resource and effectiveness in application. A more positive cathodic peak (E_{pc} = 0.78 V *vs.* RHE), onset (E_{onset} = 1.09 V *vs.* RHE) and half wave potentials ($E_{1/2}$ = 0.98 V *vs.* RHE) for the ORR and notable potential to achieve the threshold current density ($E_{@10\ mA\ cm^{-2}}$= 1.84 V *vs.* RHE) for OER are features promising to reduce overpotentials during ORR and OER. Small Tafel slopes, methanol tolerance and acceptable short term stability augment the electrocatalytic properties of the as-prepared nanocomposite. Remarkable electrocatalytic features are attributed to the synergistic effect from the mesoporous 3D framework and transition metal–organic composition. Template directed growth, tunable porosities, novel architecture and excellent electrocatalytic performance of the manganese MOF @rGO nanocomposite make it an excellent candidate for energy applications.

1. Introduction

Growing global demand for clean energy has triggered extensive research in developing next generation energy storage and conversion devices like metal–air batteries and fuel cells which can ensure an ample amount of electrical energy with trifling environmental implications.[1–3] Oxygen reduction and evolution reactions (ORR & OER) play a key role in harvesting energy from metal–air (M–air) batteries and polymer electrolyte membrane fuel cells (PEMFCs).[4] In M–air batteries, the electrocatalyst material is deposited on a porous current collector *e.g.* nickel foam or carbon paper and acts as an air-cathode for driving discharge (ORR) and charging (OER) chemistries.[5–7] In PEMFCs, it acts both as anode and cathode and primarily functions to accelerate ORR kinetics for maximizing power outputs.[8]

Commercially available noble metal catalysts, *i.e.* carbon supported Pt nanoparticles (NPs) for ORR, RuO_2 and IrO_2 for OER, have limited natural resources which hamper large scale manufacturing of these technologies.[9–11] Additionally, these catalysts lack sufficient stability and bifunctional activity for ORR & OER which sometimes leads to combining two individual catalysts to achieve bifunctionality especially for M–air batteries.[11,12] Engineering bifunctional moieties within tailored designs of catalyst frameworks is still to be envisaged and realized to capitalize on these promising electrochemical concepts. Hence, need of low-cost, efficient and stable electrocatalysts is surging in order to provide modern solutions to prevailing challenges of climate change.[13–15]

Various novel designs of nanomaterials with striking chemistries have been investigated for bifunctional purpose in the past few years. Composites of transition metal oxides,[13,16–22] sulfides,[23] nitrides,[24] carbides,[25,26] and phosphides,[27] carbon nanotubes,[28] free standing 3D graphene,[29] transition metal–organic frameworks (MOF), their derivatives and composites,[30–38] and metal free nanostructures[39] are among those NPs which have shown great potential for electrocatalytic application. Amongst all, metal–organic framework derived electrocatalysts are a class of emerging materials offering tuneable

[a]*U.S.-Pakistan Center for Advanced Studies in Energy, National University of Sciences and Technology, Islamabad 44000, Pakistan. E-mail: abdul_che06@scme.nust.edu.pk; naseem@uspcase.nust.edu.pk*

[b]*School of Chemical and Materials Engineering, National University of Sciences and Technology, Islamabad 44000, Pakistan*

† Electronic supplementary information (ESI) available. See DOI: 10.1039/d0ra04193a

functionalities, chemical, mechanical and thermal stabilities with diverse morphologies. Xia *et al.*[40] devised a strategy to synthesize hollow N-doped carbon nanotube frameworks (NCNTFs) derived from single zeolite imidazolate framework (ZIF-67) precursor suitable for oxygen electrocatalysis. Liu *et al.*[41] reported fabrication of double shelled nano-caged electrocatalyst derived from pyrolyzing ZIF-8@ZIF-67 core–shell. Likewise, Liu *et al.*[42] fabricated sandwich-like N-doped porous carbon @graphene through carbonization of ZIF-8@GO hybrid composite.

Manganese-based compounds have gained attention due to their promising potential to carry out electron transfer reactions. MnO_2 grown on carbonized ZIF-67 skeleton has shown remarkable ORR activity but OER electroactivity has not been established.[43] Although significant progress has been made in this area still many Mn-MOF based systems need special attention to unriddle their electrocatalytic capabilities.

Manganese benzene-1,4-dicarboxylate (MnBDC) is a coordination polymer formed of Mn–O–C rod-like secondary building units. It is found in monoclinic crystal structure occupying *C*2/*c* space group. Two types of manganese atoms arrange separately in MnO_6 octahedral geometry where one type utilizes oxygen atoms of six 1,4-BDC molecules while second uses oxygen atoms of five 1,4-BDC and one DMF molecule. This 3D net-like pcu arrangement of atoms offers numerous binding, catalytic and temporary storage sites viable for electrocatalytic applications.[44,45] Manganese benzene-1,4-dicarboxylate (MnBDC),[46] MnBDC@graphene[47] and their derivative MnO/C @rGO[48] have been reported as excellent anode materials for lithium ion batteries. But oxygen electrocatalytic properties of these compounds remain largely unidentified.

Herein, we report thermally reduced mesoporous MnBDC@rGO nanocomposite as promising bifunctional electrocatalyst for ORR and OER. It has been synthesized by GO-templated facile solvothermal synthesis technique followed by high temperature thermal reduction (also known as annealing) in argon gas environment. GO sheets acted as porous skeleton onto which manganese ions and clusters aligned and coordinated with incoming ligand. By annealing the nanocomposite at maximum thermal stability limit of MnBDC two objectives were achieved: (1) thermal reduction of GO into rGO by removing basal and terminal oxygen functional groups and (2) thermal activation of MnBDC MOF by increasing oxygen vacancies arising from elimination of bridged DMF molecules. It increased electronic conductivity, specific surface area and rigidity of nanocomposite leaving behind oxygen deficient structure of catalytically active manganese ions. Moreover, it introduced structural defects enabling temporary storage of redox species. Amount of GO in nanocomposite was varied to determine the effect of rGO substrate on overall performance of catalyst. Prepared catalyst material was benchmarked against commercial Pt/C with respect to cathodic peak, onset and half wave potentials, current densities and Tafel slopes of ORR performance curves. OER activities, methanol tolerance and the amperometric behaviour of catalyst have been studied as well.

2. Experiment section

2.1 Chemicals

All chemicals and reagents used for experiments were of analytical quality. Potassium permanganate ($KMnO_4$, extra pure 99–100%) manganese chloride monohydrate ($MnCl_2 \cdot H_2O$, ≥97% pure) and terephthalic acid ($C_8H_6O_4$, ≥98%) were purchased from Sigma-Aldrich. Graphite powder (chemical pure) and hydrogen peroxide (H_2O_2, 30%) were provided by Daejung, Korea. Sulfuric acid (H_2SO_4, ≥98%) and hydrochloric acid (HCl, 35.4%) were supplied by BDH AnalaR® England. Orthophosphoric acid (H_3PO_4, 85%) and methanol (CH_4O, ≥99.7%) were supplied by Honeywell, Germany. Absolute ethanol by AnalaR® NORMAPUR, VWR and *N*,*N*-dimethylformamide (C_3H_7NO, 99%) by Merck. Deionized water at 2.0 MΩ cm^{-1} resistivity was used during synthesis process. Liquid ionic binder Nafion ($C_{23}H_{20}N_2O_2S$) solution (5 wt% in methanol) was purchased from Ion Power, Inc. Commercial carbon-supported Pt NPs catalyst (10% Pt/C) was supplied by Alfa Aesar, USA.

2.2 Synthesis of graphene oxide

Graphene oxide was synthesized following improved Hummer's method as reported[49–51] with a few modifications. Briefly, 2 g (1 wt equivalent) of graphite was added to 400 mL mixture (9 : 1) of sulfuric and phosphoric acids with continuous stirring. Then, 18 g (9 wt equivalent) of $KMnO_4$ was added slowly in nine equal portions. Upon addition of $KMnO_4$, greenish black colour of slurry started changing to dark brown and slightly exothermic reaction took place. Temperature was maintained around 35–40 °C by shifting reaction vessel to ice bath. This mixture was retained at 50 °C for 3 days (72 hours) for extended oxidation.[52] Upon oxidation, reaction mixture appeared to be reddish brown in colour which was quenched by H_2O_2. The colour of mixture changed to yellow brown which was subjected to multiple washing with HCl, DI water and ethanol. A dark brown product was obtained.

2.3 Synthesis of manganese benzene 1,4-dicarboxylate (MnBDC)

As reported,[46] 0.86 g (6 mmol) of $MnCl_2 \cdot H_2O$ and 0.83 g (5 mmol) of terephthalic acid were dissolved in 40 mL *N*,*N*-dimethylformamide (DMF) with vigorous stirring. Then, 10 mL methanol was added which turns the solution transparent. The solution contained 32 mg of MOF precursor per mL of solvent mixture. It was transferred to 100 mL Teflon-lined stainless-steel autoclave and heated at 120 °C for 24 hours with temperature ramp of 3 °C min^{-1}. Crystals of manganese benzene-1,4-dicarboxylate were obtained after filtration which were dried at 80 °C overnight in vacuum oven. Product obtained was 0.91 g.

2.4 Synthesis of MnBDC@rGO nanocomposites

Different MnBDC@rGO nanocomposites (25, 50 and 75% GO) were prepared varying the amount of GO template. Briefly, a certain amount GO in proportion with MnBDC product batch size was added to 4 : 1 volumetric mixture of DMF and

methanol and ultrasonicated for 1 hour to obtain uniform dispersion. This dispersion contained 20 mg GO per mL of solvent mixture. Manganese chloride monohydrate and terephthalic acid in 6 : 5 molar ratio were dissolved in DMF under vigorous stirring and methanol was added to achieve complete solubility. MnBDC precursor solution contained 32 mg precursor per mL of solvent mixture. MOF precursor solution was slowly added to GO dispersion and sonicated for another 30 min. The reaction mixture was transferred to 100 mL autoclave and kept at above mentioned conditions. After filtration and methanol washing, nanocomposite was dried at 80 °C in vacuum oven overnight.

Obtained solid was grinded in agate mortar pestle for 30 min and shifted to alumina boat for inert argon environment annealing (thermal reduction) inside tube furnace. All the solids were annealed (thermally reduced) at 400 °C for 2.5 hours at 2 °C min^{-1} temperature ramp.

2.5 Material characterization

Crystalline phases of material were identified from X-ray diffraction patterns obtained using Bruker D8 Advance X-ray Diffractometer with Cu Kα emitted radiations (V = 40 kV, I = 30 mA, P = 1200 W and λ = 1.548 Å). Thermogravimetric analysis (TGA) profiles of samples were obtained using Discovery TGA 5500 by TA Instruments. Morphology and elemental analysis were obtained by using scanning electron microscope images and energy dispersive X-ray spectrometry from TESCAN VEGA3 scanning electron microscope (HV = 20 kV, beam intensity = 11) equipped with EDS Detector by Oxford Instruments. Types of bonding present on molecular level were analysed by Fourier transform infrared spectrum obtained by CARY 630 FTIR Spectrometer. N_2 adsorption/desorption isotherms of as-synthesized samples were acquired from Quantachrome NovaWin instrument. The Brunauer–Emmet–Teller (BET) method was employed to calculate surface area while the Barret–Joyner–Halinda (BJH) method was employed to calculate pore size distribution.

2.6 Electrochemical measurements

Catalyst ink was prepared by the following procedure. 5 mg catalyst was added to 800 μL DI water, 150 μL ethanol and 50 μL Nafion solution (5 wt% in methanol) in V : V : V = 16 : 3 : 1 respectively and dispersed by 6 hours long ultrasonication. Prior to ink loading, glassy carbon disk electrode (GC, 3 mm diameter) and platinum rotating disk electrode (RDE) were polished with 1.0, 0.3 and 0.05 micron alumina slurries. Electrodes were ultrasonicated in DI water to remove residual alumina particles. 5 μL of ink was drop casted on each electrode and dried at 50 °C for 20 min. Catalyst loadings on GC and RDE were approximately 0.35 mg cm^{-2} each. Catalyst ink of commercial Pt/C catalyst prepared in the same manner was used to benchmark ORR and OER measurements.

All electrochemical measurements were recorded on Bipotentiostat electrochemical workstation (CH Instruments Model 760E) with three electrode cell and rotating ring disk electrode assembly (RRDE-3A, CH Instruments Inc.). Silver Ag/AgCl (3 M KCl) and platinum wire were used as reference and counter electrodes respectively while catalyst loaded GC and RDE as working electrodes. All potential values were reported as V as RHE, where $E_{(RHE)} = E_{(Ag/AgCl)} + 0.059 \times pH + 0.210$. Before electrochemical tests, N_2 gas was flown through electrolyte solution to purge any entrapped atmospheric oxygen gas and saturate with inert gas. For ORR/OER test, O_2 was bubbled through electrolyte to saturate KOH solutions. For ORR test, O_2 saturated 0.1 M KOH solution was used and cyclic voltammetry profiles were recorded at different scan rates (50, 25, 20, 15, 10 and 5 mV s^{-1}) in potential window of 0.2–1.2 V. Linear sweep voltammetry measurements were carried out at 10 mV s^{-1} scan rate with different rotation speeds (100–2500 rpm). To examine current retention of catalyst over time, the amperometric i–t curve was obtained at 0.6 V with 1600 rpm in 0.1 M KOH. To determine methanol tolerance (fuel cross-over durability) of catalyst, 0.5 M methanol was added to 0.1 M KOH and CV was recorded. OER tests were carried out in O_2 saturated 1 M KOH solution where LSV was obtained at 5 mV s^{-1} scan rate in 1–1.9 V potential window at 1600 rpm. The amperometric i–t response was logged at 1.7 V again at 1600 rpm. Electrochemical impedance spectroscopy (EIS) technique was used to determine solution resistance by Nyquist plot in 0.1 Ω to 1 MΩ ohm range with amplitude 0.005 V. This resistance was then applied for iR-correction of obtained OER test data.

3. Results and discussion

XRD patterns and TGA profiles of prepared samples have been shown in Fig. 1. Fig. 1(a) presents diffraction peaks recorded for as-synthesized graphene oxide. A broad and intense characteristic peak around 9.7° is attributed to (001) plane of oxidized graphite with 8 Å interlayer distance.[49,53] A small peak at 26.1° corresponds to (002) plane of residual unreacted graphite.[54] Fig. 1(b) shows diffraction patterns of reference manganese terephthalate dihydrate (PDF# 00-035-1678), as-synthesized manganese benzene-1,4-dicarboxylate (MnBDC) and MnBDC@75% GO nanocomposite.[46–48] All the major peaks (2θ = 9.45°, 14.39°, 18.39°, 19.28°, 28.77°, 29.75°, 33.54°) can be clearly observed in both MnBDC and its composite. Purity of MnBDC phase has been confirmed by Fig. 1(b). Fig. 1(c) shows XRD pattern of annealed MnBDC MOF and thermally reduced nanocomposite (MnBDC@75% rGO). Upon heat treatment at 400 °C for 2.5 hours in continuous flow of argon gas, loosely bound and weakly coordinated linker molecules (1,4-BDC) undergo decomposition to possible smaller aromatic compounds (benzoic acid and benzophenone).[55] Peaks of MnBDC, benzoic acid, benzophenone and rGO phases have been designated with diamond (◇), dot (●), circle (○) and asterick (*) signs respectively. One peak at smaller angle prior to characteristic peak of MnBDC can be ascirbed to benzoic acid. Peak of benzophenone can be noticed around 11°. Peak intensities of decomposition products suggest that their amounts are fairly small. While most of the characteristic peaks of MnBDC are still intact, assuring the presence of MnBDC phase at annealing (thermal reduction) temperature. Peak near 27° emerges due to thermally reduced graphene oxide.[56]

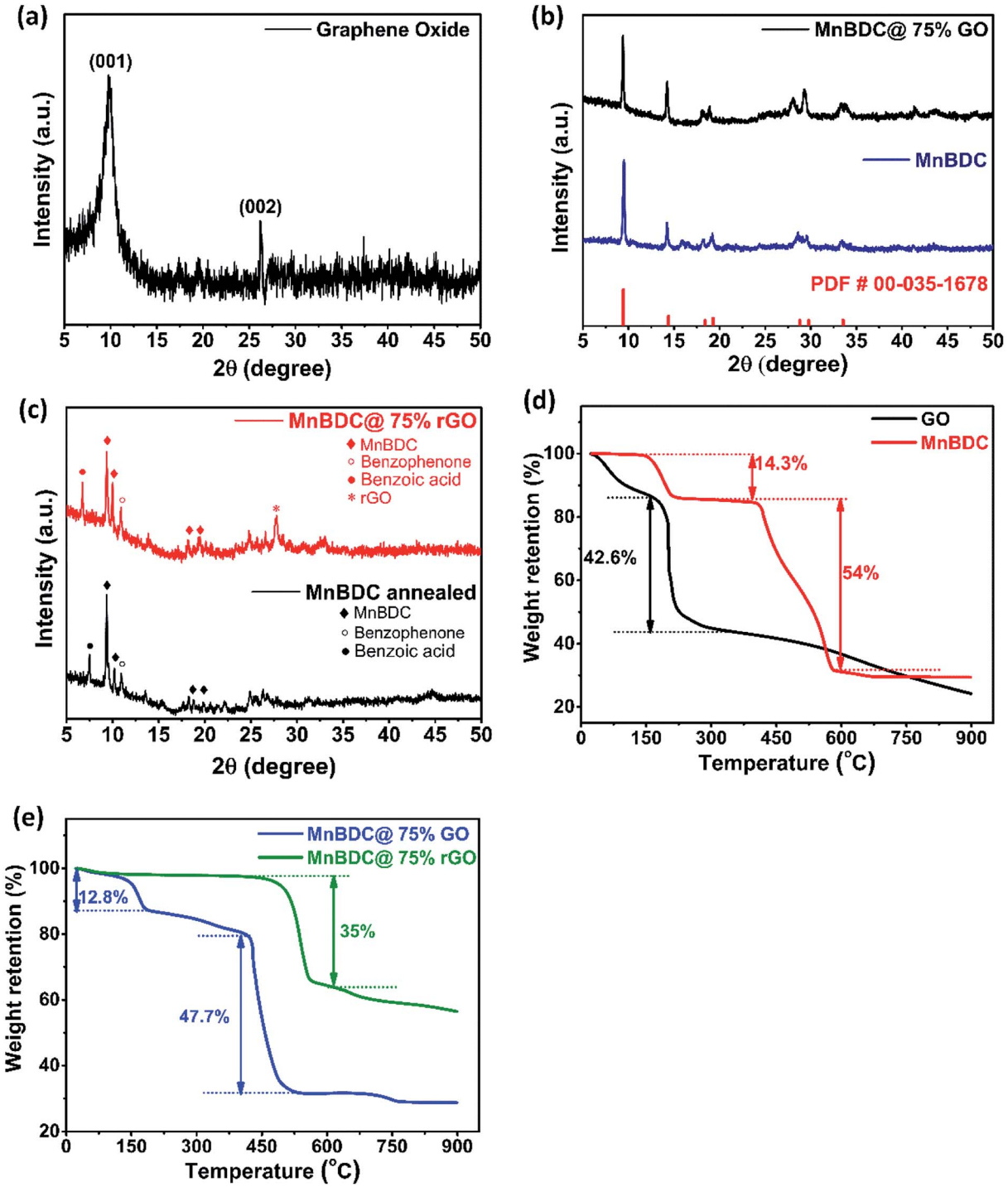

Fig. 1 XRD patterns of (a) synthesized graphene oxide, (b) MnBDC (blue), MnBDC@75% GO composite (black) along with reference pattern of manganese terephthalate (red), (c) post annealing sample of MnBDC@75% rGO (red) and MnBDC (black). TGA curves of (d) GO (black), MnBDC (red), (e) MnBDC@75% GO (blue) and MnBDC@75% rGO (green).

Fig. 1(d) displays TGA profiles of pure GO and MnBDC MOF. GO undergoes some intial mass loss due to the removal of moisture and residual acid molecules around 100 °C. From 150–220 °C, terminal oxygen functional groups formed during oxidation of graphite in improved Hummer's method start breaking away rapidly producing CO, CO_2 and small hydrocarbons. From 220–350 °C, a gradual mass loss takes place due to disruption of more stable epoxides present within the stacked GO sheets. This phenomenon creates immense amount of gas pressure in the GO interlayers which eventually leads to unstacking of GO into rGO sheets giving rise to strucural defects and conductive sp^2 hybridized structure. About

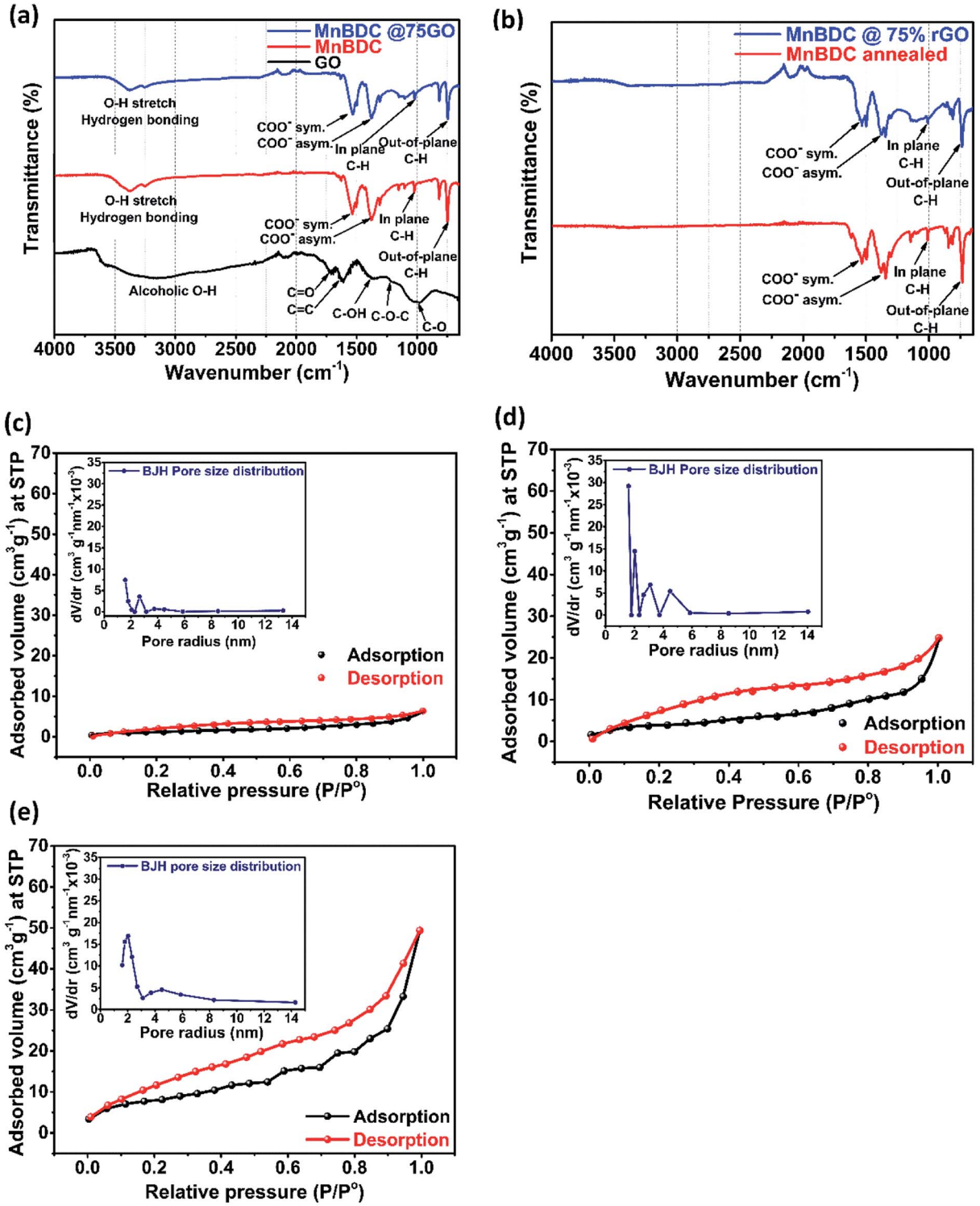

Fig. 2 FTIR spectra of (a) GO (black), MnBDC (red), MnBDC@75% GO (blue), (b) post annealing samples of MnBDC (red) and MnBDC@75% rGO (blue). N_2 sorption isotherm along with BJH pore size distribution profile as inset of (c) MnBDC, (d) MnBDC@75% GO and (e) MnBDC@75% rGO.

42.6% mass loss has been observed during thermal reduction of GO till 400 °C. Similar mass loss behavior for GO has been reported by Dattakumar *et al.*[57] For MnBDC, initial 14.3% mass loss occurs due to evaporation of moisture and coordinated DMF molecules upto 200 °C. Then, no apparent mass change occurs till 430 °C confirming its stability. An abrupt mass loss from 450 °C to 580 °C is associated with chemical decomposition of MOF into manganese oxide and porous carbon structure as reported.[48] Fig. 1(e) demonstrates TGA profiles of MnBDC@75% GO and MnBDC@75% rGO. As shown, initial

Table 1 BET surface area and BJH pore size distribution of synthesized catalyst materials

Sample	BET surface area ($m^2\ g^{-1}$)	Pore volume ($cm^3\ g^{-1}$)	Pore radius (nm)
MnBDC	4.383	0.008	1.588
MnBDC@75% GO	13.655	0.029	1.590
MnBDC@75% rGO	28.359	0.064	2.015

12.8% mass loss in MnBDC@75% GO can be ascribed to elimination of residual solvent of solvothermal synthesis and terminal oxygen groups. Then, a steady mass loss continues till 400 °C happening due to removal of basal oxygen groups of GO. A steep mass loss of 47.7% in 450–525 °C range shows decomposition of metal–organic framework to porous carbon structure. An interesting observation has been taken into account while comparing TGA profiles of pure GO shown Fig. 1(d) and MnBDC@75% GO shown in Fig. 1(e). Pure GO has undergone 57% mass loss up to 400 °C while MnBDC@75% GO has lost only 19.6% of its mass. This phenomenon can be elucidated by solvothermal conditions of MnBDC@75% GO synthesis. During synthesis, GO was added as a dispersion of DMF and methanol into MOF precursor solution and subjected to 120 °C in a closed Teflon lined autocalve for 24 hours. The *in situ* high pressure developed in the solvothermal conditions along with reducing DMF solvent and metal salts moderately reduce GO into rGO. Reduction of GO results in layer segregation or unstacking. However, degree of reduction during this step is mediocre and considerable amount of strong functional groups are still present. It is verified by TGA analysis depict 19.6% mass loss for MnBDC@75% GO till 400 °C. For complete reduction of nanocomposite, facile thermal reduction method was employed which is evident in Fig. 1(e). MnBDC@75% rGO exhibits thermal stability upto 470 °C with no apparent mass loss. It confirms that complete reduction of GO into rGO has been accomplished through thermally reducting MnBDC@75% GO nanocomposite. Moreover, DMF and weak linker coordinations in MnBDC@75% rGO have also disappeared activating catalyst material for desired application.

FTIR spectra and N_2 sorption isotherms have been shown in Fig. 2. Fig. 2(a) displays molecular fingerprint of GO, MnBDC and MnBDC@75% GO which is quite relatable with literature.[46,58] GO exhibits characteristic infrared frequency bands of O–H bond (ν_{O-H} at 3550–3200 cm^{-1}) of alcoholic hydroxyl group, C=O double bond ($\nu_{C=O}$ at 1710 cm^{-1}), C=C double bond ($\nu_{C=C}$ at 1617 cm^{-1}), C–O–H bond (ν_{C-O-H} at 1365 cm^{-1}), C–O–C bond (ν_{C-O-C} at 1214 cm^{-1}) and C–O single bond (ν_{C-O} at 1042 cm^{-1}) of corresponding carboxyl and carbonyl groups. These moities are present scarcely on basal plane but mostly along the edges of 2D sheets. MnBDC shows presence of 4 prominent frequency bands of carboxylic group. Frequency bands at 1533 cm^{-1} and 1378 cm^{-1} appear due to symmetric and asymmetric stretching vibrations of carboxyl C=O respectively. While in-plane and out-of-the-plane C–H bonds linked with benzene ring appear at 1020 cm^{-1} and 745 cm^{-1} respectively. This out-of-the plane bond confirms coordination of linker with manganese ions within framework as reported.[46] Moreover, O–H stretching vibrations of weak hydrogen bonding interactions of coordinated DMF solvent have been observed as two closely located peaks centered at 3378 cm^{-1} and 3252 cm^{-1}. In Fig. 2(b), FTIR spectra of annealed MnBDC and MnBDC@75% rGO nanocomposite (thermally reduced) have been shown. It is interesting to note that both the samples in Fig. 2(b) namely annealed MnBDC and MnBDC@75% rGO have lost stretching vibrations in the high frequency region (3000–3500 cm^{-1}). Peaks of O–H vibration due to hydrogen bonding have completely vanished from both samples indicating absolute removal of coordinated DMF solvent molecules from pore internals. Actually, DMF molecules form coordination with Mn ions and 1,4-BDC linker molecules during crystallizations of MOF and get entrapped inside porous structure. All other characteristic bands are still present without any significant shift which confirms the integrity and stability of framework at thermal reduction temperature. It proves that annealing (thermal reduction) has successfully removed O–H bonds creating oxygen deficiency within the framework which were previously occupied by coordinated DMF. In MnBDC@75% rGO along with DMF solvent disappearance of major oxygen group has taken place indicating that terminal as well as basal oxygen functional groups have been stripped off. FTIR spectra validate our initial proposition of annealing at high temperature to synthesized oxygen deficient structure with embedded structural defect capable of providing catalytically active and temporary storage sites for redox species.

Fig. 2(c), (d) and (e) show N_2 adsorption desorption isotherms of MnBDC, MnBDC@75% GO and MnBDC@75% rGO respectively where inset plots represent BJH pore size distributions. Here, we used desorption part of the isotherm for pore size distribution plots. All the isotherms resemble type-IV hysteresis loop indicating presence of mesopores. Area enclosed by isotherms increases in order of MnBDC, MnBDC@75% GO and MnBDC@75% rGO. Surface area, pore radius and pore volume of MnBDC are 4.383 $m^2\ g^{-1}$, 1.588 nm and 0.008 $cm^3\ g^{-1}$ respectively which are lowest of all three samples. Poor porosity arises from pore passivation by DMF molecules which penetrate porous structure and develop coordination during MOF crystallization. They occupy voids and reduce adsorption area resulting in low porosity. In case of MnBDC@75% GO, the addition of GO has roughly increased surface area by three folds to 13.655 $m^2\ g^{-1}$ because of its instrinsic high surface area of lamellar structure. Despite the prepared GO is mainly present in aggregated form of stacked sheet, it improves surface area of composite significantly. Pore radius and pore volume of MnBDC@75% GO are 1.59 nm and 0.029 $cm^3\ g^{-1}$ respectively. Pore size of nanocomposite is unaffected even after the addition of GO because of same DMF coordination issue inside pores but pore volume has risen in accordance with surface area attributable to GO. In case of MnBDC@75% rGO, surface area and porosity have surprising improved as a result of thermal redution of GO and pore activation of MnBDC MOF. Surface area, pore radius and pore volume of MnBDC@75% rGO are 28.359 $m^2\ g^{-1}$, 2.015 nm and

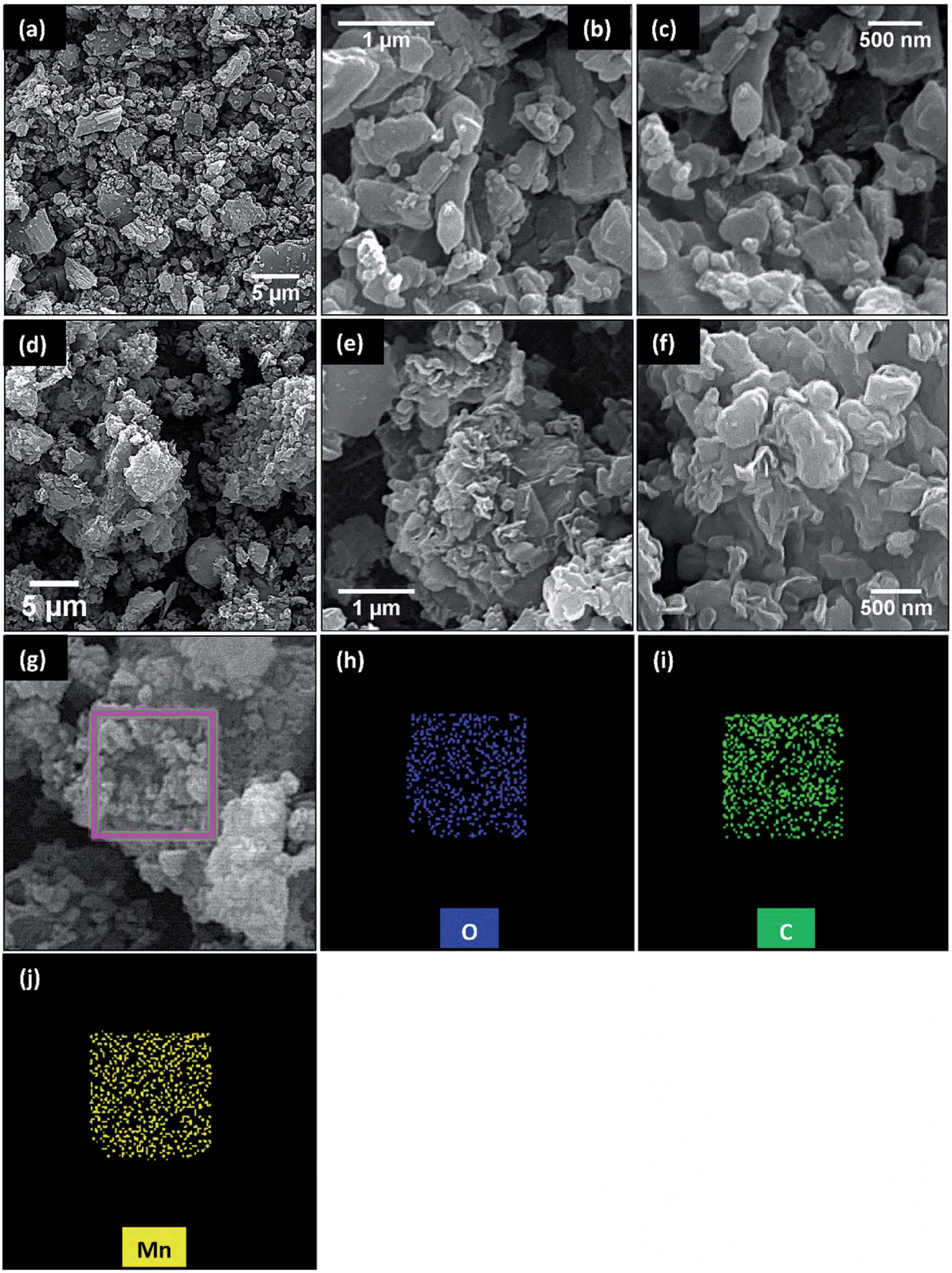

Fig. 3 SEM micrographs of (a–c) annealed MnBDC and (d–f) MnBDC@75% rGO. EDS elemental mapping of (g–j) MnBDC@75% rGO with (h) oxygen, (i) carbon and (j) manganese maps.

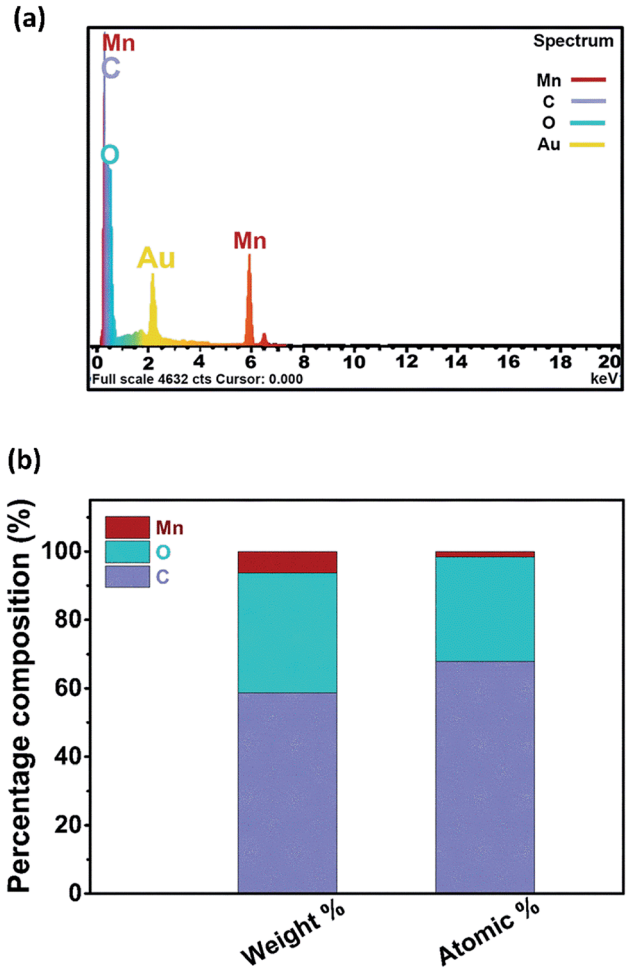

Fig. 4 (a) Energy dispersive X-ray spectroscopy (EDS) of MnBDC@75% rGO and (b) percentage compositions of detected elements presented graphically.

0.064 $cm^3\ g^{-1}$ respectively. Striking increments of 107%, 27% and 120% have been calculated in surface area, pore size and pore volume after thermal reduction of nanocomposite. BET surface areas and BJH pore size distributions of samples have been summarized in Table 1.

Structural and morphological features of samples explored by scanning electron microscope have been shown in Fig. 3. For comparison, micrographs of pristine metal–organic framework (*i.e.* MnBDC) after annealing have been displayed in Fig. 3(a–c). MnBDC having monoclinic crystal structure, as reported,[44] occupies *C*2/*c* space group. Manganese atoms arrange in MnO_6 octahedral geometries. Mn–O–C secondary building units in corners and edges connect together to form 3D net like framework. Here, distorted network of crystals appears due to removal of bridged DMF molecules which is highly favorable for electrocatalysis. Fig. 3(d–f) are SEM micrographs of thermally reduced MnBDC@75% rGO. It is noticeable that particles are fabricated onto GO template and even after thermal reduction, no disruptions of layers has taken place. It infers that GO reduction during solvothermal synthesis had sufficiently unstacked aggregated GO sheets and thermal reduction did not damage nanocomposite integrity. It confirms that GO has served the purpose of self-templated growth of nanocomposite. We conducted elemental mapping of MnBDC@75% rGO and detected all three major elements namely Mn, O and C within framework fairly uniform distribution as shown in Fig. 3(g–j). For quantitative elemental analysis of MnBDC@75% rGO, energy dispersive X-ray spectroscopy was applied and results are shown in Fig. 4. Mn, O and C were detected as major elements. No considerable amount of any impurity was observed in this analysis as shown in Fig. 4(a). Fig. 4(b) shows graphical representation of the results received through EDS where average weight and atomic percentages of elements have been shown as stacked bar graphs. Weight percentages of Mn, O and C are 6.33%, 34.97% and 58.89% respectively. Atomic percentages of Mn, O and C are 1.61%, 30.47% and 67.92% respectively.

To evaluate the electrocatalytic activities of the prepared samples for oxygen reduction reaction (ORR), cyclic voltammetry tests were performed in N_2/O_2 saturated aqueous alkaline 0.1 M KOH electrolyte solution. Fig. 5(a) displays cyclic voltammograms of Pt/C commercial, MnBDC@75% rGO, MnBDC@50% rGO, MnBDC@25% rGO and MnBDC (annealed) in N_2 and O_2 saturated 0.1 M KOH solution as dotted and continuous lines respectively. As evident, no reduction peak for any of the catalyst sample can be seen in N_2 saturated solution. While for O_2 saturated solution, distinct cathodic peaks for ORR have been observed. As we know that, the more positive the reduction potential, the better electrocatalytic activity expected from the material. ORR peak potentials of 0.61 V for MnBDC, 0.72 V for MnBDC@25% rGO, 0.75 V for MnBDC@50% rGO, 0.78 V for MnBDC@75% rGO and 1.03 V for Pt/C commercial have gradually shifted towards more positive potential indicating improvement in electrocatalytic performance with subsequent increase in the amount of rGO. However, ORR potential of Pt/C is still highest of all showing superior catalytic activity. It is noteworthy that the area of CV curves is concomitantly increasing with rising rGO content in the nanocomposite. Larger CV area gives higher specific capacitance which is directly related to electrochemically active and specific surface areas. It imparts better electroactivity to catalyst material. CV area and specific surface area of prepared catalyst come in great agreement. MnBDC@75% rGO has exhibited high BET surface area so its CV curve area is also large. *Vice versa* can be noted for MnBDC sample. Similar trend is being followed in case of cathodic peak current densities. Best current densities have been recorded as 0.70 mA cm^{-2} for MnBDC@75% rGO and 2.12 mA cm^{-2} for Pt/C commercial.

To further examine the ORR activities of samples, linear sweep voltammetry (LSV) tests were performed using rotating disk working electrode (RDE). Fig. 5(b) demonstrates LSV curves of Pt/C commercial, MnBDC@75% rGO, MnBDC@50% rGO, MnBDC@25% rGO and MnBDC at 1600 rpm rotational speed in O_2 saturated 0.1 M KOH. Onset potentials have shown same trend as of cathodic peak potential and a gradual rise in E_{onset} proves improvement in ORR activity with corresponding increase in rGO amount. ORR activity of MnBDC@75% rGO coincides with Pt/C commerical as revealed by onset potentials. E_{onset} of MnBDC@75% rGO and Pt/C are estimated to be 1.09 V

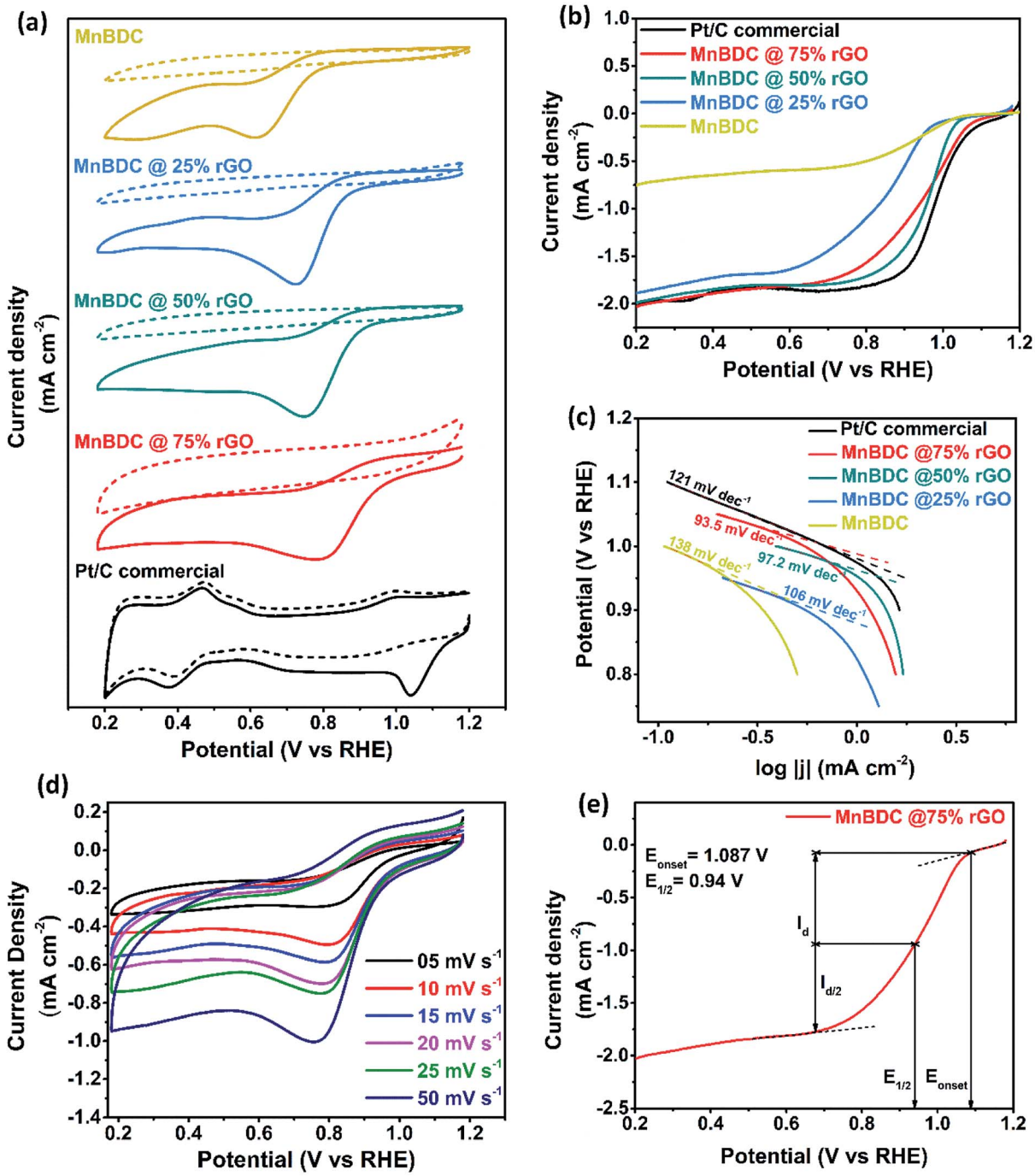

Fig. 5 (a) CV profiles of Pt/C commercial (black), MnBDC@75% rGO (red), MnBDC@50% rGO (green), MnBDC@25 rGO (blue) and MnBDC (yellow) in N_2 (dot line) and O_2 (continuous line) saturated 0.1 M KOH solution. (b) LSV profiles of Pt/C commercial (black), MnBDC@75% rGO (red), MnBDC@50% rGO (green), MnBDC@25 rGO (blue) and MnBDC (yellow) in O_2 saturated 0.1 M KOH solution at 1600 rpm rotation with 10 mV s^{-1} scan rate. (c) Tafel plots of Pt/C commercial (black), MnBDC@75% rGO (red), MnBDC@50% rGO (green), MnBDC@25 rGO (blue) and MnBDC (yellow) labelled with respective slope values. (d) CV profiles of MnBDC@75% rGO at different scan rates 5–50 mV s^{-1} in O_2 saturated 0.1 M KOH solution. (e) LSV profile of MnBDC@75% rGO at 1600 rpm in O_2 saturated 0.1 M KOH with 10 mV s^{-1} scan.

and 1.10 V respectively. Most useful information here is provided by maximum current density of LSV curves. Maximum current densities of MnBDC, MnBDC@25% rGO, MnBDC@50% rGO and MnBDC@75% rGO are received in increasing order as 0.75 V, 1.88 V, 1.98 V and 2.03 V respectively reflecting improvement in ORR activity. MnBDC@75% rGO has delivered exactly same current density as by Pt/C (2.03 mA cm^{-2}) which implies that at higher diffusion rates ORR activities of both Pt/C commercial and MnBDC@75% rGO catalysts are equated. Half wave potentials of both the catalysts are also

Table 2 Cathodic peak potential, peak current densities and Tafel slopes of prepared samples

Sample	E_{pc} (V)	J_{pc} (mA cm^{-2})	Tafel slope (mV dec^{-1})
Pt/C	1.04	2.12	121
MnBDC@75% rGO	0.78	0.70	93.5
MnBDC@50% rGO	0.75	0.54	97.2
MnBDC@25% rGO	0.72	0.45	106
MnBDC	0.61	0.40	138

Table 3 Summary of onset potentials, half-wave potentials and maximum current densities calculated from LSVs of prepared samples

Sample	E_{onset} (V)	$E_{1/2}$ (V)	J_{max} (mA cm^{-2})
Pt/C	1.10	0.98	2.03
MnBDC@75% rGO	1.09	0.94	2.03
MnBDC@50% rGO	1.07	0.96	1.98
MnBDC@25% rGO	0.99	0.85	1.88
MnBDC	1.04	0.91	0.75

comparable (0.98 V for Pt/C and 0.94 V for MnBDC@75% rGO). MnBDC has exhibited anomalous higher E_{onset} and $E_{1/2}$ potentials but poor current densities overshadow these aspect of MnBDC resulting in low ORR activity.

Tafel plot and Tafel slope are semi-quantitative parameter which give a rough estimation about the polarization behavior of catalyst for ORR. Electrode polarization is a common phenomenon arising from increasing resistence in catalyzing ORR. High Tafel slope indicates high overpotentials encountered during ORR while low Tafel slope predicts to achieving high current densities with low overpotentials hinting at faster ORR kinetics. Tafel plots for MnBDC, MnBDC@25% rGO, MnBDC@50% rGO, MnBDC@75% rGO and Pt/C commercial with measured slopes 138 mV dec^{-1}, 106 mV dec^{-1}, 97.2 mV dec^{-1}, 93.5 mV dec^{-1} and 121 mV dec^{-1} have been shown in Fig. 5(c). MnBDC@75% rGO is least suffered from high overpotential problem for ORR confirming its faster reaction kinetics. Again, a gradual decline in slope value has been received with increasing amount of rGO. To inspect the consistency of reduction potential, CV at different scan rates (5–50 mV s^{-1}) was conducted and obtained curves have been displayed in Fig. 5(d) which reveals that no obvious shift in reduction peak has been observed. Peak current densities in the CV curves of MnBDC@75% rGO increased with corresponding increase in scan rate. This behavior is in accordance with Randles–Sevcik equation which represents direct proportionality between peak current and scan rate. Fast scan rates cause concentration gradient of electroactive species on the surface of electrode and high currents are generated in CV. Fig. 5(e) represents LSV of MnBDC@75% rGO with measured values of onset and half-wave potentials. A summary of electrochemical performance parameters of ORR activity for MnBDC, MnBDC@25% rGO, MnBDC@50% rGO, MnBDC@75% rGO and Pt/C commercial catalysts has been tabulated in Tables 2 and 3.

In order to have a better insight of electroactivity of MnBDC@75% rGO, a series of LSV tests were conducted with varying rotational speeds of RDE from 100–2500 rpm and shown in Fig. 6(a). While onset potentials remain largely unaffected, diffusion limiting current increases with increasing rotation speed due to better mass diffusion at high speed. These LSV curves were obtained at constant scan rate of 10 mV s^{-1} and used to draw Koutecky–Levich plot in the Fig. 6(b). Linearity of K–L plots obtained at various potential values (0.3–0.7 V) confirms first order kinetics of oxygen reduction reaction.

Fuel cross-over is a common occurrence for fuel cell and other electrochemical applications. Examining durability of material against methanol is considered beneficial for ensuring feasibility of bifunctional electrocatalyst. For that, 0.5 M CH_3OH was added to 0.1 M KOH solution. The results have been shown in Fig. 6(c). Pt/C does not show stability upon methanol addition and prominent peak of methanol oxidation appears which eclipses oxygen reduction commonly termed as methanol poisoning. Contrarily, MnBDC@75% rGO shows no signs of methanol oxidation which provides evidence of methanol tolerance. Position of cathodic peak is unaffected by methanol but a small loss (15%) in ORR peak current density has been recorded. Amperometric current–time response of Pt/C and MnBDC@75% rGO has also been shown in Fig. 6(d). Pt/C retains 83% of initial current delivered after 5000 s of test while MnBDC@75% rGO shows current retention up to 54%. It confirms that our catalyst material performs well in short term durability test. Fig. 6(e) shows ORR polarization curves of MnBDC@75% rGO. A significant amount of current (65%) can be retrieved even after 2500 cycles of CV which suggests that catalyst can efficiently deliver current for more than thousand cycles while retaining considerable current density.

Electrochemical active surface area (ECSA) of prepared MnBDC@75% rGO was evaluated from cyclic voltammetry (CV) of sample in 1 M KOH solution. CVs at eight different potential scan rates (0.005–0.8 V s^{-1}) around open circuit potential (OCP) of three electrode cell have been displayed in Fig. 7(a). Anodic and cathodic currents with respect to applied scan rates were linear fitted as shown in Fig. 7(b) in order to estimate double layer capacitance (C_{DL}) of catalyst loaded electrode surface as reported.[59] Average value of slopes of linear fits applied on anodic and cathodic currents is regarded as C_{DL}. Specific capacitance (C_s) was calculated from closed polygon area of CV in N_2 saturated 1 M KOH solution. Both C_{DL} and C_s were used to calculate ECSA of catalyst loaded on electrode surface. Fig. 7(c) exhibits electrochemical impedance spectroscopy (EIS) of bare working electrode and equivalent circuit fitting where circuit fitting was simulated to estimate electrolyte solution resistance. This solution resistance value (R_s) allowed us to compensate ohmic drop occurring due to mass transfer resistance of electrolyte. Ohmic *iR* correction was done simply by *E-iR* factor. Fig. 7(d) demonstrates OER activities of prepared MnBDC@75% rGO and commercial Pt/C catalysts with the help of LSV profile obtained in 1 M KOH solution. MnBDC@75% rGO catalyst achieved 10 mA cm^{-2} current density at 1.84 V

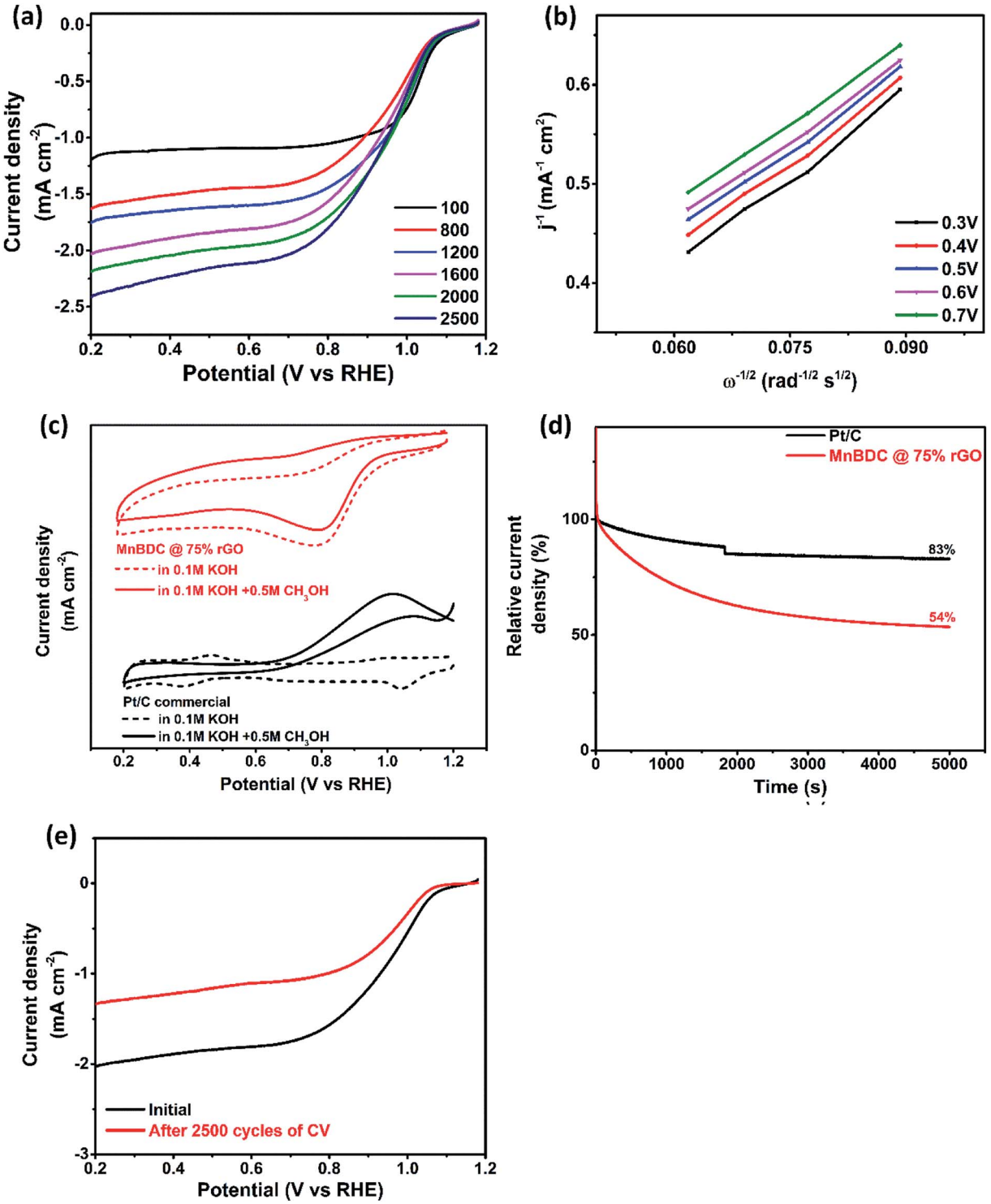

Fig. 6 (a) LSV profiles of MnBDC@75% rGO at different rotation speeds 100–2500 rpm with 10 mV s^{-1} scan rate in O_2 saturated 0.1 M KOH. (b) Koutecky–Levich plot of MnBDC@75% rGO at different potential values (0.3–0.7 V). (c) CV profiles of Pt/C (black) and MnBDC@75% rGO (red) in 0.1 M KOH (dot line) and O.1 M KOH + 0.5 M CH_3OH (continuous line) solutions. (d) The amperometric *i–t* response of Pt/C (black) and MnBDC@75% rGO (red). (e) ORR polarization curves of MnBDC@75% rGO before (black) and after 2500 cycles of CV (red).

versus 1.89 V for Pt/C. Tafel slopes in Fig. 7(e) of both catalysts also indicate that MnBDC@75% rGO is superior electrocatalyst with smaller Tafel slope (83 mV dec^{-1} and 149 mV dec^{-1} respectively). Smaller slope confirms that prepared catalyst is capable of achieving same current *i.e.* 10 mA cm^{-2} at lower overpotential. Electrochemical stability of MnBDC@75% rGO was confirmed by the amperometric *i–t* response with lower current drop occurring over time as shown in Fig. 7(f).

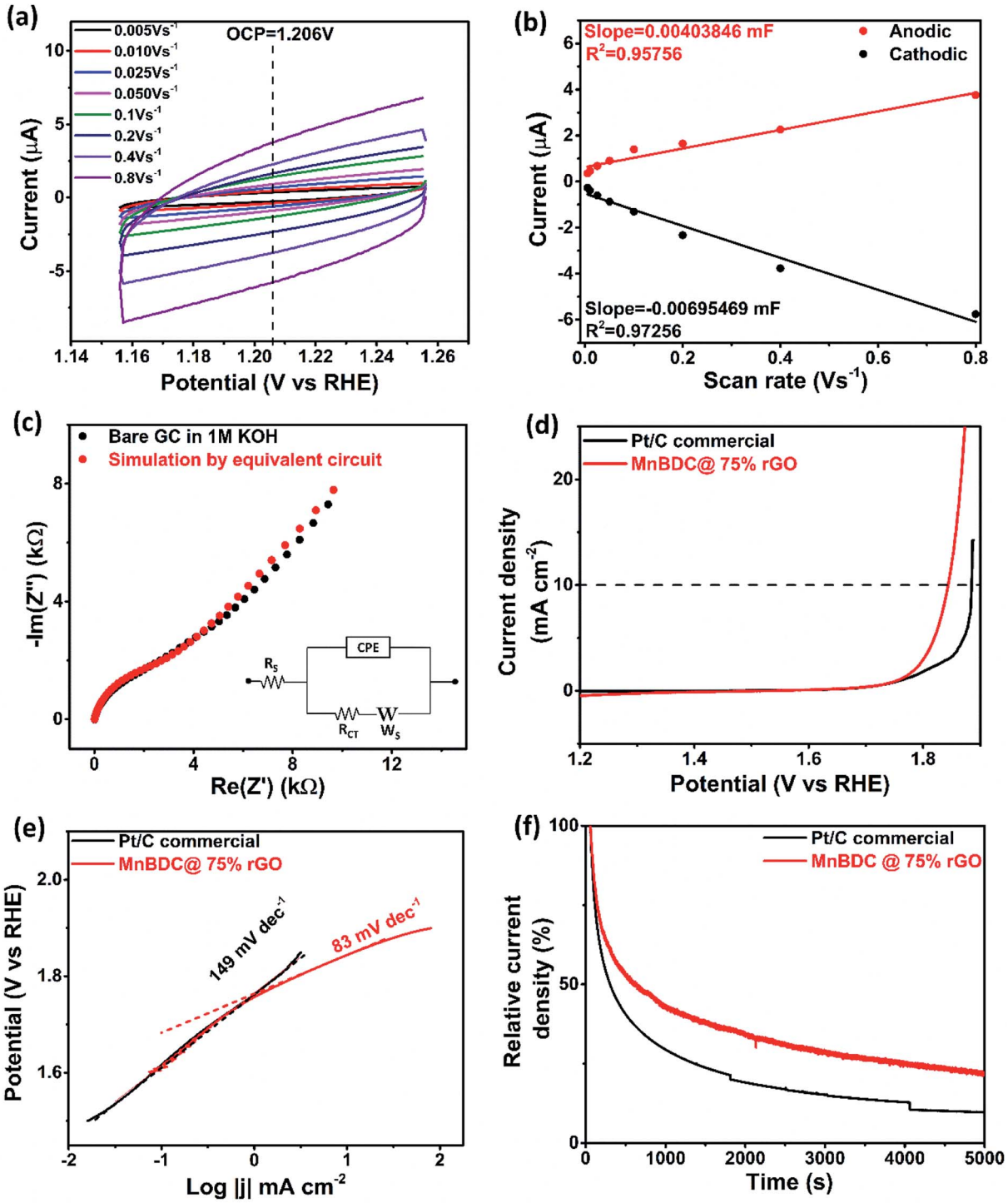

Fig. 7 (a) CV profiles of MnBDC@75% rGO at 8 different scan rates in 0.1 V potential window around open circuit potential (1.206 V) in 1 M KOH. (b) Anodic and cathodic currents at OCP w.r.t different potential scans (0.005–0.8 V s^{-1}) of CV plotted along with linear fitting. (c) Electrochemical impedance spectroscopy of bare working electrode in 1 M KOH electrolyte (black) along with simulation through equivalent circuit fitting (red). (d) LSV profiles of Pt/C (black) and MnBDC@75% rGO (red) in 1 M KOH solution for OER measurement. (e) Tafel plots of Pt/C (black) and MnBDC@75% rGO (red) obtained from LSV profiles. (f) The amperometic *i*–*t* response of Pt/C (black) and MnBDC@75% rGO (red) at 1.7 V.

Moreover, there were no current fluctuations happening for MnBDC@75% rGO as compared to Pt/C commercial. Remarkable electrochemical properties can be ascribed to synergistic effect from favourable elemental composition of transition metal complex and mesoporous layered morphology. Manganese ions facilitate electron transfer during reversible redox reactions while oxygen deficient mesoporous layered structure provides mass diffusion and charge transfer. Thus,

electrochemical redox species form and decompose more frequently resulting in low overpotentials of ORR and OER and high current densities. In short, MnBDC@75% rGO provides excellent bifunctional electrocatalyst material for applications in metal–air batteries and fuel cell. Its synthesis involves few simple steps, its porosities and functionalities can be easily tuned and morphology can be altered with the help of templated growth and it can be potentially employed as suitable electrocatalyst for oxygen electrocatalytic applications in energy storage systems.

Conclusion

GO template assisted fabrication of MnBDC MOF has been successfully implemented to synthesize manganese MOF and graphene oxide nanocomposites with variable GO amounts (25%, 50% and 75%). Thermal reduction of the samples was carried at high temperature (400 °C) in an inert environment continuously flowing argon gas yielding three samples MnBDC@25% rGO, MnBDC@50% and MnBDC@75% rGO. This thermal treatment has been found beneficial in activating nanocomposites by removing all strongly coordinated solvent molecules which might degrade catalyst's quality. Out of the prepared electrocatalysts, MnBDC@75% rGO exhibits good bifunctional activity for ORR and OER in aqueous alkaline electrolyte solutions. It offers good onset, half-wave and cathodic peak potentials during LSV and CV tests comparable to Pt/C commercial catalyst for ORR activity. Tafel slope of MnBDC@75% rGO is lowest of all catalysts studies in this work showing low overpotential for achieving high current density. MnBDC@75% rGO has been found stable in methanol fuel cross over tests and shows no oxidation peaks for methanol as compared to Pt/C which is strongly poisoned by methanol and ORR activity is compromised. For OER, MnBDC@75% rGO achieves threshold current density of 10 mA cm^{-2} at lower potential as compared to Pt/C along with smaller Tafel slope. Nanocomposite synthesized through this approach can incorporate desired structural features like mesoporous surface, controlled growth and tuneable functionalities. Our best catalyst MnBDC@75% rGO exhibits low overpotentials for ORR and OER and the acceptable amperometric response against time. Moreover, this synthesis scheme can be easily implemented to fabricate nanocomposites of other MOFs.

Conflicts of interest

Authors declare no competing financial interests.

References

1 S. Yang, P. He and H. Zhou, Research progresses on materials and electrode design towards key challenges of Li-air batteries, *Energy Storage Mater.*, 2018, **13**, 29–48.
2 K. Surya, M. S. Michael and S. R. S. Prabaharan, A review on advancement in non-noble metal based oxides as bifunctional catalysts for rechargeable non-aqueous Li/air battery, *Solid State Ionics*, 2018, **317**, 89–96.
3 Z. Chen, D. Higgins, A. Yu, L. Zhang and J. Zhang, A review on non-precious metal electrocatalysts for PEM fuel cells, *Energy Environ. Sci.*, 2011, **4**, 3167–3192.
4 B. Zhu, D. Xia and R. Zou, Metal–organic frameworks and their derivatives as bifunctional electrocatalysts, *Coord. Chem. Rev.*, 2018, **376**, 430–448.
5 J. Gao, X. Cai, J. Wang, M. Hou, L. Lai and L. Zhang, Recent progress in hierarchically structured O2-cathodes for Li-O_2 batteries, *Chem. Eng.*, 2018, **352**, 972–995.
6 D. Aurbach, B. D. McCloskey, L. F. Nazar and P. G. Bruce, Advances in understanding mechanisms underpinning lithium–air batteries, *Nat. Energy*, 2016, **1**, 16128.
7 H. F. Wang and Q. Xu, Materials design for rechargeable metal–air batteries, *Matter*, 2019, **1**, 565–595.
8 S. Hanif, X. Shi, N. Iqbal, T. Noor, R. Anwar and A. M. Kannan, ZIF derived PtNiCo/NC cathode catalyst for proton exchange membrane fuel cell, *Appl. Catal., B*, 2019, **258**, 117947.
9 S. Jiang, K. Ithisuphalap, X. Zeng, G. Wu and H. Yang, 3D porous cellular $NiCoO_2$/graphene network as a durable bifunctional electrocatalyst for oxygen evolution and reduction reactions, *J. Power Sources*, 2018, **399**, 66–75.
10 M. Guo, Y. Li, L. Zhou, Q. Zheng, W. Jie, F. Xie and D. Lin, Hierarchically structured bimetallic electrocatalyst synthesized *via* template-directed fabrication MOF arrays for high-efficiency oxygen evolution reaction, *Electrochim. Acta*, 2019, **298**, 525–532.
11 M. K. Debe, Electrocatalyst approaches and challenges for automotive fuel cells, *Nature*, 2012, **486**, 43–51.
12 J. C. Meier, I. Katsounaros, C. Galeano, H. J. Bongard, A. A. Topalov, A. Kostka, A. Karschin, F. Schüth and K. J. J. Mayrhofer, Stability investigations of electrocatalysts on the nanoscale, *Energy Environ. Sci.*, 2012, **5**, 9319–9330.
13 Y. Liu, Y. Liu, S. H.-S. Cheng, S. Yu, B. Nan, H. Bian, K. Md, M. Wang, C. Y. Chung and Z.-G. Lu, Conformal coating of heterogeneous CoO/Co nanocomposites on carbon nanotubes as efficient bifunctional electrocatalyst for Li-air batteries, *Electrochim. Acta*, 2016, **219**, 560–567.
14 S. Lin, Y. Li, S. Luo, X. Ren, L. Deng, H. Mi, P. Zhang, L. Sun and Y. Gao, 3D-ordered porous nitrogen and sulfur Co-Doped carbon supported PdCuW nanoparticles as efficient catalytic cathode materials for Li-O_2 batteries, *Electrochim. Acta*, 2018, **272**, 33–43.
15 H. Gong, H. Xue, T. Wang, H. Guo, X. Fan, L. Song, W. Xia and J. He, High-loading nickel cobaltate nanoparticles anchored on three-dimensional N-doped graphene as an efficient bifunctional catalyst for lithium–oxygen batteries, *ACS Appl. Mater. Interfaces*, 2016, **8**, 18060–18068.
16 M. Yuan, Y. Yang, C. Nan, G. Sun, H. Li and S. Ma, Porous Co_3O_4 nanorods anchored on graphene nanosheets as an effective electrocatalysts for aprotic Li–O_2 batteries, *Appl. Surf. Sci.*, 2018, **444**, 312–319.
17 Z. Song, X. Qin, N. Cao, X. Gao, Q. Liang and Y. Huo, Mesoporous CoO/reduced graphene oxide as bi-functional catalyst for Li–O_2 battery with improved performances, *Mater. Chem. Phys.*, 2018, **203**, 302–309.

18 C. Luo, H. Sun, Z. Jiang, H. Guo, M. Gao, M. Wei, Z. Jiang, H. Zhou and S.-G. Sun, Electrocatalysts of Mn and Ru oxides loaded on MWCNTS with 3D structure and synergistic effect for rechargeable Li-O_2 battery, *Electrochim. Acta*, 2018, **282**, 56–63.

19 J. H. Kim, Y. J. Oh and Y. C. Kang, Design and synthesis of microporous $(Mn_{1/3}Co_{2/3})O$-carbon nanotubes composite microspheres as efficient catalysts for rechargeable Li–O_2 batteries, *Carbon*, 2018, **128**, 125–133.

20 J. Zhang, L. Wang, L. Xu, X. Ge, X. Zhao, M. Lai, Z. Liu and W. Chen, Porous cobalt–manganese oxide nanocubes derived from metal–organic frameworks as a cathode catalyst for rechargeable Li–O_2 batteries, *Nanoscale*, 2015, **7**, 720–726.

21 A. Pendashteh, J. Palma, M. Anderson and R. Marcilla, $NiCoMnO_4$ nanoparticles on N-doped graphene: highly efficient bifunctional electrocatalyst for oxygen reduction/evolution reactions, *Appl. Catal., B*, 2017, **201**, 241–252.

22 H. Jang, A. Zahoor, Y. Kim, M. Christy, M. Y. Oh, V. Aravindan, Y. S. Lee and K. S. Nahm, Tailoring three dimensional α-MnO_2/RuO_2 hybrid nanostructure as prospective bifunctional catalyst for Li–O_2 batteries, *Electrochim. Acta*, 2016, **212**, 701–709.

23 Z. Zhang, X. Wang, G. Cui, A. Zhang, X. Zhou, H. Xua and L. Gu, $NiCo_2S_4$ sub-micron spheres: an efficient nonprecious metal bifunctional electrocatalyst, *Nanoscale*, 2014, **6**, 3540–3544.

24 Y. Hang, C. Zhang, X. Luo, Y. Xie, S. Xin, Y. Li, D. Zhang and J. B. Goodenough, α-MnO_2 nanorods supported on porous graphitic carbon nitride as efficient electrocatalysts for lithium–air batteries, *J. Power Sources*, 2018, **392**, 15–22.

25 J.-S. Li, S.-L. Li, Y.-J. Tang, M. Han, Z.-H. Dai, J.-C. Bao and Y.-Q. Lan, Nitrogen-doped Fe/Fe_3C@graphitic layer/carbon nanotube hybrids derived from MOFs: efficient bifunctional electrocatalysts for ORR and OER, *Chem. Commun.*, 2015, **51**, 2710–2713.

26 R. Gao, Y. Zhou, X. Liu and J. Wang, N-doped defective carbon layer encapsulated W_2C as a multifunctional cathode catalyst for high performance Li–O_2 battery, *Electrochim. Acta*, 2017, **245**, 430–437.

27 J. Li, G. Liu, B. Liu, Z. Min, D. Qian, J. Jiang and J. Li, An extremely facile route to Co_2P encased in N,P-codoped carbon layers: Highly efficient bifunctional electrocatalysts for ORR and OER, *Int. J. Hydrogen Energy*, 2018, **43**, 1365–1374.

28 R. E. Fuentes, H. R. Colón-Mercado and E. B. Fox, Electrochemical evaluation of carbon nanotubes and carbon black for the cathode of Li-air batteries, *J. Power Sources*, 2014, **255**, 219–222.

29 M. He, P. Zhang, L. Liu, B. Liu and S. Xu, Hierarchical porous nitrogen doped three-dimensional graphene as free-standing cathode for rechargeable lithium–oxygen batteries, *Electrochim. Acta*, 2016, **191**, 90–97.

30 H. B. Wu and X. W. Lou, Metal–organic frameworks and their derived materials for electrochemical energy storage and conversion: Promises and challenges, *Sci. Adv.*, 2017, **3**, eaap9252.

31 B. Zhu, D. Xia and R. Zou, Metal–organic frameworks and their derivatives as bifunctional Electrocatalysts, *Coord. Chem. Rev.*, 2018, **376**, 430–448.

32 S. Dang, Q.-L. Zhu and Q. Xu, Nanomaterials derived from metal–organic frameworks, *Nat. Rev. Mater.*, 2018, **4**, 17075.

33 M. Guo, Y. Li, L. Zhou, Q. Zheng, W. Jie, F. Xie, C. Xu and D. Lin, Hierarchically structured bimetallic electrocatalyst synthesized *via* template-directed fabrication MOF arrays for high-efficiency oxygen evolution reaction, *Electrochim. Acta*, 2019, **298**, 525–532.

34 I. S. Amiinu, X. Liu, Z. Pu, W. Li, Q. Li, J. Zhang, H. Tang, H. Zhang and S. Mu, From 3D ZIF nanocrystals to Co–N_x/C nanorod array electrocatalysts for ORR, OER, and Zn–Air batteries, *Adv. Funct. Mater.*, 2018, **5**, 1704638.

35 T. Fan, F. Yin, H. Wang, X. He and G. Li, A metal–organic-framework/carbon composite with enhanced bifunctional electrocatalytic activities towards oxygen reduction/evolution reactions, *Int. J. Hydrogen Energy*, 2017, **42**, 17376–17385.

36 D. Yu, P. R. Ilango, S. Han, M. Ye, Y. Hu, L. Li and S. Peng, Metal–organic framework derived Co@NC/CNT hybrid as a multifunctional electrocatalyst for hydrogen and oxygen evolution reaction and oxygen reduction reaction, *Int. J. Hydrogen Energy*, 2019, **44**, 32054–32065.

37 S. Hanif, N. Iqbal, X. Shi, T. Noor, G. Ali and A. M. Kannan, NiCo–N-doped carbon nanotubes based cathode catalyst for alkaline membrane fuel cell, *Renewable Energy*, 2020, **154**, 508–516.

38 S. A. M. Rizvi, N. Iqbal, M. D. Haider, T. Noor, R. Anwar and S. Hanif, Synthesis and characterization of Cu-MOF derived Cu@AC electrocatalyst for oxygen reduction reaction in PEMFC, *Catal. Lett.*, 2020, **150**, 1397–1407.

39 J. Zhang, Z. Zhao, Z. Xia and L. Dai, A metal-free bifunctional electrocatalyst for oxygen reduction and oxygen evolution reactions, *Nat. Nanotechnol.*, 2015, **10**, 444–452.

40 B. Y. Xia, Y. Yan, N. Li, H. B. Wu, X. W. Lou and X. Wang, A metal–organic framework-derived bifunctional oxygen electrocatalyst, *Nat. Energy*, 2016, **1**, 15006.

41 S. Liu, Z. Wang, S. Zhou, F. Yu, M. Yu, C.-Y. Chiang, W. Zhou, J. Zhao and J. Qiu, Metal–organic-framework-derived hybrid carbon nanocages as a bifunctional electrocatalyst for oxygen reduction and evolution, *Adv. Mater.*, 2017, **29**, 1700874.

42 S. Liu, H. Zhang, Q. Zhao, X. Zhang, R. Liu, X. Ge, G. Wang, H. Zhao and W. Cai, Metal–organic framework derived nitrogen-doped porous carbon@graphene sandwich-like structured composites as bifunctional electrocatalysts for oxygen reduction and evolution reactions, *Carbon*, 2016, **106**, 74–83.

43 J.-X. Zhang, L.-N. Zhou, J. Chen, X. Yin, W.-T. Kuang and Y.-J. Li, Co^{II}-catalyzed room-temperature growth of MnO_2 on the skeleton of carbonized zeolitic imidazolate framework-67 crystals for boosting oxygen reduction reaction, *J. Mater. Chem. A*, 2019, **7**, 4699–4704.

44 F. Luo, Y.-X. Che and J.-M. Zheng, Construction of microporous metal–organic frameworks (MOFs) by Mn–O–C rod-like secondary building units (SBUs): Solvothermal

synthesis, structure, thermostability, and magnetic properties, *Inorg. Chem. Commun.*, 2018, **11**, 358–362.

45 S. Li, Y. Dong, J. Zhou, Y. Liu, J. Wang, X. Gao, Y. Han, P. Qi and B. Wang, *Energy Environ. Sci.*, 2018, **11**, 1318–1325.

46 H. Hu, X. Lou, C. Li, X. Hu, T. Li, Q. Chen, M. Shen and B. Hu, A thermally activated manganese 1,4-benzenedicarboxylate metal–organic framework with high anodic capability for Li-ion batteries, *New J. Chem.*, 2016, **40**, 9746–9752.

47 S. He, Z. Li, L. Ma, J. Wang and S. Yang, Graphene oxide-templated growth of MOFs with enhanced lithium-storage properties, *New J. Chem.*, 2017, **41**, 14209–14216.

48 X.-M. Tian, D.-L. Zhao, W.-J. Meng, X.-Y. Han, H.-X. Yang, Y.-J. Duan and M. Zhao, Highly porous MnO/C@rGO nanocomposite derived from Mn-BDC@rGO as high-performance anode material for lithium ion batteries, *J. Alloys Compd.*, 2019, **792**, 487–495.

49 D. C. Marcano, D. V. Kosynkin, J. M. Berlin, A. Sinitskii, Z. Sun, A. Slesarev, L. B. Alemany, W. Lu and J. M. Tour, Improved synthesis of graphene oxide, *ACS Nano*, 2010, **4**, 8.

50 N. I. Zaaba, K. L. Foo, U. Hashim, S. J. Tan, W.-W. Liu and C. H. Voon, Synthesis of graphene oxide using modified hummers method: Solvent influence, *Procedia Eng.*, 2017, **184**, 469–477.

51 M. D. P. Lavin-Lopez, A. Romero, J. Garrido, L. Sanchez-Silva and J. Valverde, Influence of different improved hummers method modifications on the characteristics of graphite oxide in order to make a more easily scalable method, *Ind. Eng. Chem. Res.*, 2016, **55**, 12836–12847.

52 L. Zhang, J. J. Liang, Y. Huang, Y. F. Ma, Y. Wang and Y. S. Chen, Size-controlled synthesis of graphene oxide sheets on a large scale using chemical exfoliation, *Carbon*, 2009, **47**, 3365–3368.

53 A. Jabbar, G. Yasin, W. Q. Khan, M. Y. Anwar, R. M. Korai, M. N. Nizam and G. Muhyodin, Electrochemical deposition of nickel graphene composite coatings: effect of deposition temperature on its surface morphology and corrosion resistance, *RSC Adv.*, 2017, **7**, 31100–31109.

54 L. Zhang, J. Liang, Y. Huang, Y. Ma, Y. Wang and Y. Chen, Size-controlled synthesis of graphene oxide sheets on a large scale using chemical exfoliation, *Carbon*, 2009, **47**, 3365–3380.

55 Y. Jing and W. Jiming, Thermal decomposition behavior of terephthalate in inert gas, *China Pet. Process. Petrochem. Technol.*, 2017, **193**, 1–8.

56 B. Zhao, P. Liu, Y. Jiang, D. Pan, H. Tao, J. Song, T. Fang and W. Xu, Supercapacitor performances of thermally reduced graphene oxide, *J. Power Sources*, 2012, **198**, 423–427.

57 D. Mhamane, S. M. Unni, A. Suryawanshi, O. Game, C. Rode, B. Hannoyer, S. Kurungot and S. Ogale, Trigol based reduction of graphite oxide to graphene with enhanced charge storage activity, *J. Mater. Chem.*, 2012, **22**, 11140–11145.

58 B. D. Ossonona and D. Bélanger, Synthesis and characterization of sulfophenyl-functionalized reduced graphene oxide sheets, *RSC Adv.*, 2017, **7**, 27224–27234.

59 C. C. L. McCrory, S. Jung, J. C. Peters and T. F. Jaramillo, Benchmarking heterogeneous electrocatalysts for the oxygen evolution reaction, *J. Am. Chem. Soc.*, 2013, **135**, 16977–16987.

